Impact imaging of aircraft composite structure based on a model-independent spatial-wavenumber filter

Lei Qiu[a,b], Bin Liu[a,c], Shenfang Yuan[a*], Zhongqing Su[b]

* Corresponding author, E-mail: ysf@nuaa.edu.cn

a State Key Lab of Mechanics and Control of Mechanical Structures, Nanjing University of Aeronautics and Astronautics, Nanjing 210016, China.

b Department of Mechanical Engineering, The Hong Kong Polytechnic University, Kowloon, Hong Kong.

c Department of Air Force Military Transportation, Air Force Service College, Xuzhou 221000, China.

Abstract: The spatial-wavenumber filtering technique is an effective approach to distinguish Lamb wave propagating direction and wave mode in spatial-wavenumber domain. Therefore, it has been gradually studied for damage evaluation in recent years. But for on-line impact monitoring in practical application, the main problem is how to realize the spatial-wavenumber filtering of impact signal when the wavenumber of high spatial resolution can not be measured or the accurate wavenumber curve can not be modeled. In this paper, a new model-independent spatial-wavenumber filter based impact imaging method is proposed. In this method, a 2D cross-shaped array constructed by two linear piezoelectric (PZT) sensor arrays is used to acquire impact signal on-line. The continuous complex Shannon wavelet transform is adopted to extract frequency narrowband signals from the frequency wideband impact response signals of the PZT sensors. A model-independent spatial-wavenumber filter is designed based on the spatial-wavenumber filtering technique. Based on the designed filter, a wavenumber searching and best match mechanism is proposed to implement the spatial-wavenumber filtering of the frequency narrowband signals without modeling in order to obtain a wavenumber-time image of the impact relative to a linear PZT sensor array. By using the two wavenumber-time images of the 2D cross-shaped array, the impact direction can be estimated without blind angle. The impact distance relative to the 2D cross-shaped array can be calculated by using the difference of time-of-flight between the frequency narrowband signals of two different central frequencies and the corresponding group velocities. The validations performed on a carbon fiber composite laminate plate and an aircraft composite oil tank show a good impact localization accuracy of the model-independent spatial-wavenumber filter based impact imaging method.

Keywords: Composite structure; impact imaging; Lamb wave; spatial-wavenumber filter; linear piezoelectric sensor array; aircraft composite oil tank.

1. Introduction

Composite materials have been gradually applied to aircraft important load-bearing structures [1]. Impact monitoring of aircraft composite structures has become an important research topic in the field of Structural Health Monitoring (SHM) [2]. Many investigations have been reported to realize impact monitoring by using the piezoelectric (PZT) sensor and Lamb wave based SHM technology, such as the time differences and geometry based impact location methods [3, 4], the artificial intelligent based impact location methods [5, 6], the mechanic model based impact location methods [7, 8]. However, these methods researched so far still have their own limitations of being applied to practical application.

In the past decade, Lamb wave based structural damage imaging methods have been studied widely and show a good application potential [9-19]. Therefore, several researchers began to introduce structural imaging methods to impact localization in recent years. These studies can be divided into two branches. The first branch is based on sparse PZT sensor array. Park and Chang [20] studied a structural impact energy imaging method, in which, the time domain transfer functions of Lamb wave signals propagating on the monitored structure were obtained by combining a pre-impact experiment performed on the structure with a finite element model of the structure. When impact response signals were acquired, the impact energy distribution image of the whole structural plane can be obtained based on the transfer functions. The position of the maximum impact energy can be judged to be the impact position. In Meo and Ciampa's research [21], the pre-impact experiment and a frequency narrowband acoustic emission sensor were used to acquire the frequency domain transfer functions of frequency narrowband impact response signals propagating on the monitored structure. When impact response signals were acquired during an on-line impact monitoring process, an impact image can be obtained by performing the time reversal focusing of the impact response signals based on the measured transfer functions. However, for the purpose of practical application, as well as to prevent any occurrence of damage in the structure, no pre-impact experiment is permitted to be performed beforehand. To solve this problem, Qiu and Yuan [22] proposed a phase synthesis time reversal focusing method for impact imaging. In this method, the frequency narrowband impact response signals were extracted from the frequency wideband impact response signals by using the continuous complex Shannon wavelet transform, and the impact position can be obtained by searching the time reversal focusing position based on the phase modulation and synthesis of the frequency narrowband signals in time domain. For the branch of dense PZT sensor array, Yuan and Zhong [23] proposed a linear PZT sensor array based multiple

signal classification method to realize impact imaging and localization. This method combined the noise subspace spanned by the time domain frequency narrowband impact response signals with the directional vector of the linear PZT sensor array to search the impact position. The frequency narrowband impact response signals were extracted by using the Gabor wavelet transform. All these methods mentioned above have shown the potential of using structural imaging method to achieve impact localization of high signal-to-noise ratio and better fault tolerance. But further researches are still needed to be performed.

Comparing with the time domain and frequency domain processing of Lamb wave signal in the methods mentioned above, the spatial-wavenumber filtering technique is an effective approach to distinguish wave propagating direction and wave mode in spatial-wavenumber domain. Thus, this technique has been gradually studied for damage evaluation in recent years [24-29]. But in most of these studies, the wavenumber of high spatial resolution of frequency narrowband Lamb wave signal must be measured by using a scanning laser Doppler vibrometer. It is not suitable for measuring the wavenumber of impact signal because the impact is an instant event. Thus, these methods can not be applied on-line. Regarding the on-line damage imaging combining with the spatial-wavenumber filter, Purekar et al [30, 31] adopted a linear PZT sensor array and a finite element modeling method to obtain frequency narrowband Lamb wave signals and the corresponding wavenumber curve respectively. Based on the wavenumber curve, a spatial-wavenumber filter was realized to be a directional filter to search the damage direction. Wang and Yuan [32] also developed this method for damage imaging of composite structure. These studies showed a high computational efficiency and damage direction estimation accuracy of this method. But for impact monitoring, the accurate wavenumber curve of the impact signal propagating on a complex composite structure is difficult to be obtained. The blind angle and near-field problem of the linear PZT sensor array should be further studied. Therefore, these above mentioned researches on the spatial-wavenumber filtering technique can not be applied for on-line impact monitoring directly at the current stage. The following four problems should be further studied. 1) How to realize the spatial-wavenumber filter when the wavenumber of high spatial resolution of impact signal can not be measured or the accurate wavenumber curve of impact signal can not be modeled. 2) For damage monitoring, the frequency narrowband Lamb wave signal can be excited by using a frequency narrowband excitation signal. But impact signal is frequency wideband. The one-to-one relationship between the wavenumber of the signal and its propagating direction can not be satisfied. 3) For damage localization, the excitation signal can be controlled and the excitation time can be considered to be a reference time to estimate the time-of-flight of damage reflections. But for impact

localization, there is no excitation reference time. 4) The monitoring area covered by a linear PZT sensor array is constrained by the angle and near-field blindness phenomenon.

To apply the dense PZT sensor array based spatial-wavenumber filtering technique for on-line impact monitoring of real aircraft composite structure, a new model-independent spatial-wavenumber filter based impact imaging method is proposed. In this method, the continuous complex Shannon wavelet transform is used to extract frequency narrowband impact response signals. A model-independent spatial-wavenumber filter is designed and a wavenumber searching and best match mechanism is proposed to implement the spatial-wavenumber filtering without wavenumber measuring or modeling. By combining with a 2D cross-shaped array constructed by two linear PZT sensor arrays, the impact localization can be realized without blind angle. Detail validations of the proposed method are performed on a carbon fiber composite laminate plate and an aircraft composite oil tank to evaluate its performance on aircraft composite structure.

The rest of this paper is organized as follows. In Section 2, the model-independent spatial-wavenumber filter based impact imaging method is proposed. In Section 3, the impact localization method based on the 2D cross-shaped array is discussed. In Section 4 and Section 5, the proposed method is validated on the composite plate and the composite oil tank respectively. Finally, the conclusion is made in Section 6.

2. Impact imaging based on a model-independent spatial-wavenumber filter

2.1. Spatial sampling

A linear PZT sensor array constructed by M PZT sensors is placed on a plate-like structure shown in Fig. 1. The PZT sensors are numbered as m=1, 2 ... M. A Cartesian coordinate is constructed on the structure. The center point of the linear PZT sensor array is set to be the origin point of the Cartesian coordinate. The distance between the centers of each two adjacent PZT sensors is Δx.

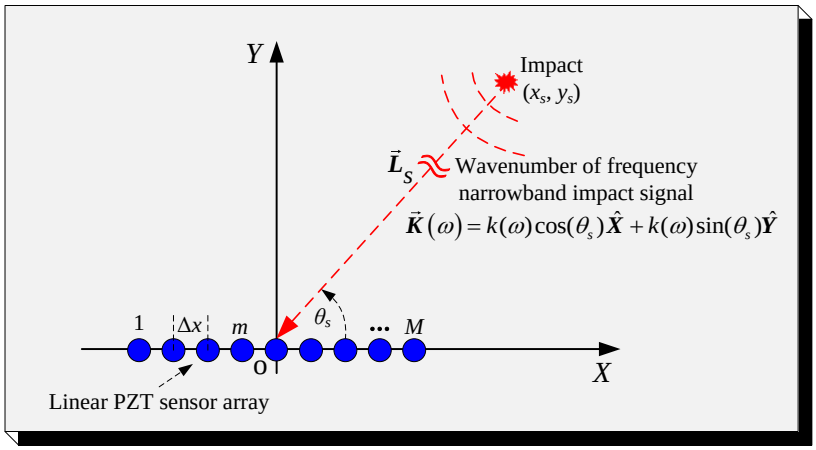

Fig. 1. Schematic diagram of the spatial sampling of a linear PZT sensor array

As shown in Fig. 1, an impact occurs and excites a frequency wideband impact signal on the plate. The position of the impact is unknown and supposed to be (x_s, y_s). The direction (angle) and the distance of the impact relative to the linear PZT sensor array are supposed to be θ_s and L_s respectively.

A frequency narrowband signal of low central frequency, which is extracted from the frequency wideband impact response signal of the PZT sensor located at (x_m, 0), can be expressed as Eq. (1) [2, 12, 33]. The central frequency of the frequency narrowband signal is set to be ω. In a thin plate-like structure, A_0 mode is dominant at low frequency [33]. Thus, the frequency narrowband signal can be approximated to be single-mode.

$$f\left(t\right)=u(t)\cdot e^{i\cdot\left(\omega\cdot t-k(\omega)\cdot\left|\vec{\boldsymbol{X}}_m-\vec{\boldsymbol{L}}_s\right|\right)}=u(t)\cdot e^{i\cdot\omega\cdot t}\cdot e^{-i\cdot k(\omega)\cdot\left|\vec{\boldsymbol{X}}_m-\vec{\boldsymbol{L}}_s\right|} \tag{1}$$

Where, $k(\omega)$ and $u(t)$ are the wavenumber and the amplitude of the frequency narrowband impact signal respectively. $\vec{\boldsymbol{L}}_S$ denotes the distance vector of L_s and $\vec{\boldsymbol{X}}_m$ denotes the distance vector of x_m, $x_m=[(2m\text{-}1)\text{-}M]\Delta x/2$. The frequency narrowband signal shown in Eq. (1) can be seen to be a time domain sampling signal, in which, t is the signal sampling time, $t=l\cdot\Delta t$. Δt is the sampling interval time. l is the sampling dot, $l=1, 2,\ldots, SL$. SL is the sampling length. The sampling rate can be denoted as $1/\Delta t$.

Supposing that the PZT sensors are located near the origin point ($x_m<<L_s$), the wavenumber related phase component in Eq. (1) can be approximated to be Eq. (2) [34-36]:

$$e^{-i\cdot k(\omega)\cdot\left|\vec{\boldsymbol{X}}_m-\vec{\boldsymbol{L}}_s\right|}\approx e^{-i\cdot k(\omega)\cdot L_s}e^{i\cdot k(\omega)\cdot\hat{\boldsymbol{L}}_s\cdot\vec{\boldsymbol{X}}_m}e^{-i\cdot k(\omega)\frac{x_m{}^2-(\hat{\boldsymbol{L}}_s\cdot\vec{\boldsymbol{X}}_m)^2}{2L_s}} \tag{2}$$

Where, $\hat{\boldsymbol{L}}_S$ denotes the unit direction vector of the $\vec{\boldsymbol{L}}_S$.

Based on Eq. (2), the time domain sampling signal shown in Eq. (1) can be rewritten to be Eq. (3) in far-field situation [34-36].

$$f\left(t\right)\approx u(t)\cdot e^{i\cdot\omega\cdot t}\cdot e^{-i\cdot k(\omega)\cdot L_s}\cdot e^{i\cdot k(\omega)\cdot\hat{\boldsymbol{L}}_s\cdot\vec{\boldsymbol{X}}_m}=A(t)\cdot e^{i\cdot k(\omega)\cdot\hat{\boldsymbol{L}}_s\cdot\vec{\boldsymbol{X}}_m} \tag{3}$$

Where $A(t)$ denotes the amplitude term of the spatial sampling signal and it is expressed as Eq. (4).

$$A(t)=u(t)\cdot e^{i\cdot\omega\cdot t}\cdot e^{-i\cdot k(\omega)\cdot L_s} \tag{4}$$

Comparing with the time domain signal sampling, the linear PZT sensor array can be also regarded as a spatial sampling device. The spatial sampling rate is $2\pi/\Delta x$. The frequency narrowband spatial sampling signal, which is acquired by the linear PZT sensor array at time t, can be represented as Eq. (5).

$$\mathbf{f}\left(x,t\right)=\left[f\left(x_1,t\right),f\left(x_2,t\right),\cdots,f\left(x_m,t\right),\cdots,f\left(x_M,t\right)\right] \tag{5}$$

By using Discrete Fast Fourier Transform (DFFT), the spatial sampling signal can be transformed to wavenumber domain, as shown in Eq. (6).

$$\begin{aligned} F\left(k,t\right) &= \sum_{x=x_1}^{x_M} A(t)\cdot e^{i\cdot k(\omega)\cdot \hat{\boldsymbol{L}}_s\cdot \bar{\boldsymbol{X}}}\cdot e^{-ikx} \\ &= A(t)\sum_{x=x_1}^{x_M} e^{i\cdot k(\omega)\cdot\cos\theta_s\cdot x}\cdot e^{-ikx} \\ &= 2\pi\cdot A(t)\cdot\delta(k-k(\omega)\cdot\cos\theta_s) \end{aligned} \tag{6}$$

Where δ is the Dirac function which is given out in Eq. (7).

$$\delta(k-k(\omega)\cdot\cos\theta_s)=\begin{cases}1 & k=k(\omega)\cdot\cos\theta_s \\ 0 & k\neq k(\omega)\cdot\cos\theta_s\end{cases} \tag{7}$$

It can be seen from Eq. (6) and Eq. (7) that the wavenumber k=$k(\omega)\cdot\cos\theta_s$ of the spatial sampling signal acquired by the linear PZT sensor array is the wavenumber $k(\omega)$ of the frequency narrowband signal projecting onto the X-axis in far-field situation. Thus, if the wavenumber $k(\omega)$ can be known beforehand, the impact direction can be estimated.

In some previous studies [30, 31], a spatial-wavenumber filter was designed based on the wavenumber $k(\omega)$ to search the direction θ_s from 0° to 180°. But in this method, the accurate wavenumber $k(\omega)$ of high spatial resolution must be obtained by mechanic modeling or finite element modeling. It is difficult to be applied to aircraft composite structure at current stage. Therefore, a model independent spatial-wavenumber filter is proposed to solve this problem.

2.2. Model-independent spatial-wavenumber filter

A model-independent spatial-wavenumber filter is designed to be Eq. (8), in which, k' is the central wavenumber of the filter. The corresponding wavenumber spectrum is expressed as Eq. (9). It indicates that the model-independent spatial-wavenumber filter has the purpose of selectively passing through the signals of wavenumber k=k', while rejecting the signals of the other wavenumbers $k\neq k'$. By applying the model-independent spatial-wavenumber filter to the spatial sampling signal, the wavenumber spectrum of the filtered signal can be obtained as Eq. (10). It can be noted that if k'=$k(\omega)\cdot\cos\theta_s$, which means that the wavenumber of the model-independent spatial-wavenumber filter is equal to the X-axis projection wavenumber of the frequency narrowband impact signal, the amplitude of the filtered signal will reach to the maximum value.

$$\boldsymbol{\phi}\left(x\right)=\left[e^{i\cdot k'\cdot x_1},e^{i\cdot k'\cdot x_2},\cdots,e^{i\cdot k'\cdot x_m},\cdots,e^{i\cdot k'\cdot x_M}\right] \tag{8}$$

$$\Phi(k)=\sum_{x=x_1}^{x_M} e^{ik'x}e^{-ikx}=2\pi\delta(k-k') \tag{9}$$

$$H'(k,t)=4\pi^2\cdot A(t)\cdot\delta(k'-k(\omega)\cdot\cos\theta_s) \tag{10}$$

Based on the model-independent spatial-wavenumber filter, a wavenumber searching and best-match mechanism is proposed to realize the spatial-wavenumber filtering of the frequency narrowband impact signal to search the value of the wavenumber $k(\omega)\cdot\cos\theta_s$. The energy of the filtered signal at the wavenumber k_n can be expressed as Eq. (11). The symbol '⊗' denotes the convolution operation between the spatial sampling signal and the model-independent spatial-wavenumber filter. The wavenumber k_n is searched from $-k_{\max}$ to $+k_{\max}$ based on Eq. (12). $k_{\max}$ is the maximum cutoff wavenumber of the spatial sampling. It is determined by the spatial sampling rate, as shown in Eq. (13). The wavenumber searching interval is denoted as Δk. n is the searching step. The maximum searching step is N determined based on Eq. (14).

$$h_{k_n}(t)=\sum\left|\mathbf{f}(x,t)\otimes\boldsymbol{\phi}_{k_n}(x)\right| \tag{11}$$

$$k_n=-k_{\max}+(n-1)\Delta k,\ \ n=1,2,\cdots,N \tag{12}$$

$$k_{\max}=\frac{1}{2}\times\frac{2\pi}{\Delta x}=\frac{\pi}{\Delta x} \tag{13}$$

$$N=(2k_{\max}/\Delta k)+1 \tag{14}$$

For a given k_n, a model-independent spatial-wavenumber filter $\boldsymbol{\phi}_{k_n}(x)$ can be generated based on Eq. (8) and the energy of the filtered signal $h_{k_n}(t)$ can be calculated based on Eq. (11). Finally, a model-independent spatial-wavenumber filtering image represented as wavenumber-time can be obtained by imaging the matrix of the filtered signals' energy which are acquired at different wavenumber k_n. The matrix is expressed as Eq. (15).

$$\mathbf{h}=\left[h_{k_1}(t),...,h_{k_n}(t),...,h_{k_N}(t)\right]_{SL\times N} \tag{15}$$

Fig. 2 shows a wavenumber-time image as an example. The wavenumber corresponding to the image point of the highest pixel value can be judged as the best-match wavenumber k_n of $k_n=k(\omega)\cdot\cos(\theta_s)$, whereas the corresponding time can be interpreted as the arrival time t_R of the frequency narrowband impact signal of central frequency ω. It should be noted that the wavenumber match error, which is defined as Eq. (20), is dependent on the actual wavenumber of the frequency narrowband impact signal. It means that if the actual

wavenumber is bigger, the wavenumber match error will be smaller. This point is important for frequency selection as discussed in Sections 4.2 and 5.2. Another point should be noted is that the arrival time t_R is not the actual time-of-flight of the impact signal because the time of the impact occurrence is unknown. In actual situation, the arrival time t_R is the propagating time with respect to signal sampling zero point in time domain.

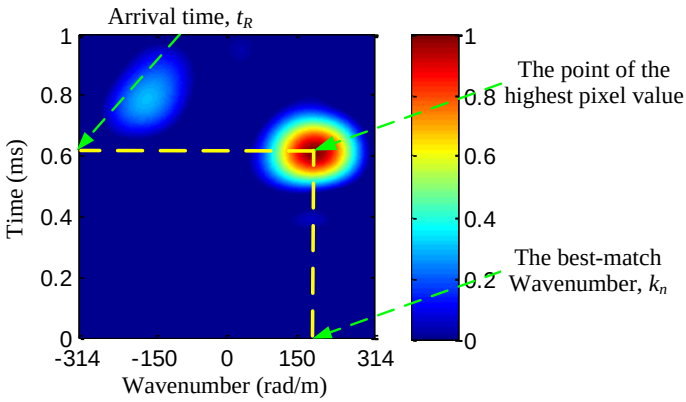

Fig. 2. An example of the wavenumber-time image

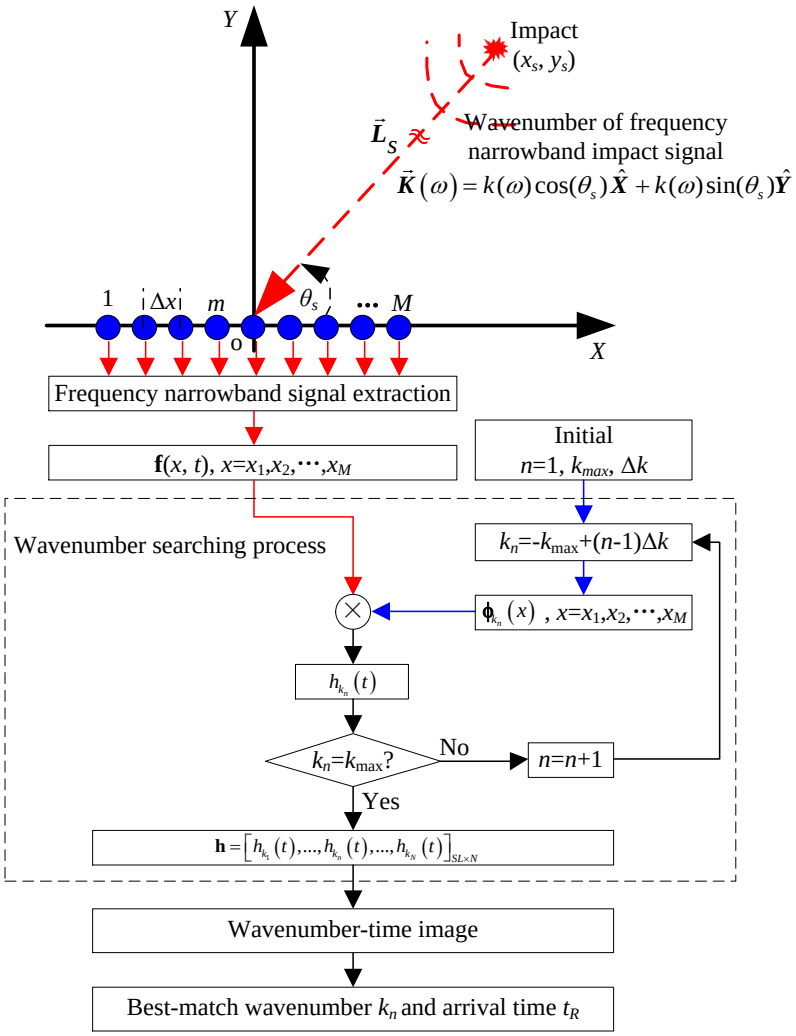

Fig. 3. Implementation process of the model-independent spatial-wavenumber filter based impact imaging method

Based on the wavenumber searching and best-match mechanism discussed above, the implementation process of the model-independent spatial-wavenumber filter based impact imaging method is shown in Fig. 3, which is summarized as follows. 1) When an impact occurs on the monitored structure, the frequency wideband impact signal is acquired by using the linear PZT sensor array. 2) The frequency narrowband impact response signals are extracted from the frequency wideband impact response signals of the PZT sensors. 3) The wavenumber searching and best-match mechanism is adopted to give out a wavenumber-time image. 4) The best-match wavenumber k_n and the arrival time t_R are obtained.

For impact direction estimation, the impact direction θ_s can be estimated based on two best-match wavenumbers obtained by using a 2D cross-shaped array. For impact distance calculation, the frequency narrowband signals of two different central frequencies are needed to be extracted from the frequency wideband impact response signals. The arrival time of the frequency narrowband signals of two different central frequencies can be obtained by using the impact imaging method respectively. Then, the impact distance L_s can be calculated based on their group velocity difference and arrival time difference. The impact localization method will be discussed in details in Section 3.

2.3. Frequency narrowband signal extraction

As mentioned above, the frequency narrowband impact response signals are needed to fulfill the spatial-wavenumber filtering and imaging. In this paper, the continuous complex Shannon wavelet transform is adopted to extract the frequency narrowband signal. It is shown in Eq. (16).

$$\mathrm{WT}(a,b) = |a|^{-\frac{1}{2}} \int_{-\infty}^{\infty} f(t)\psi_{\text{shan-}a,b}\left(\frac{t-b}{a}\right)\mathrm{d}t \tag{16}$$

Where a and b are the scale factor and time factor respectively. The complex Shannon wavelet function is defined as Eq. (17) [22]:

$$\psi_{\text{shan-}a,b}(t) = \sqrt{f_b}\,\mathrm{sinc}(f_b t)e^{2\pi i f_c t} \tag{17}$$

Where f_b and f_c are the frequency band and the central frequency of the wavelet function. The sinc function is represented as Eq. (18):

$$\mathrm{sinc}(t) = \begin{cases} 1 & t = 0 \\ \dfrac{\sin(\pi t)}{\pi t} & t \neq 0 \end{cases} \tag{18}$$

The Fourier transform of Eq. (17) can be expressed as Eq. (19). It indicates that the central frequency of the complex Shannon wavelet function is at ω_c and the frequency band is limited in the range of (ω_c−ω_b/2,

$\omega_c+\omega_b/2$]. It means that the continuous complex Shannon wavelet transform of a signal is a frequency narrowband signal of central frequency ω_c/a and frequency band ($\omega_c/a-\omega_b/2a$, $\omega_c/a+\omega_b/2a$]. The example of the frequency narrowband signal extraction will be given in section 4.2.

$$\Psi_{\text{shan-}a,b}(\omega)=\begin{cases}\sqrt{\dfrac{2\pi}{\omega_b}} & \omega_c-\dfrac{\omega_b}{2}<\omega\le\omega_c+\dfrac{\omega_b}{2}\\ 0 & \text{Others}\end{cases} \tag{19}$$

Where $\omega_b=2\pi f_b$, $\omega_c=2\pi f_c$, $\omega_c>\omega_b/2$.

3. Impact localization based on 2D cross-shaped array

A 2D cross-shaped array shown in Fig. 4 is constructed by two linear PZT sensor arrays labeled as No.I and No.II. The center point of the 2D cross-shaped array is set to be the origin point of the Cartesian coordinate.

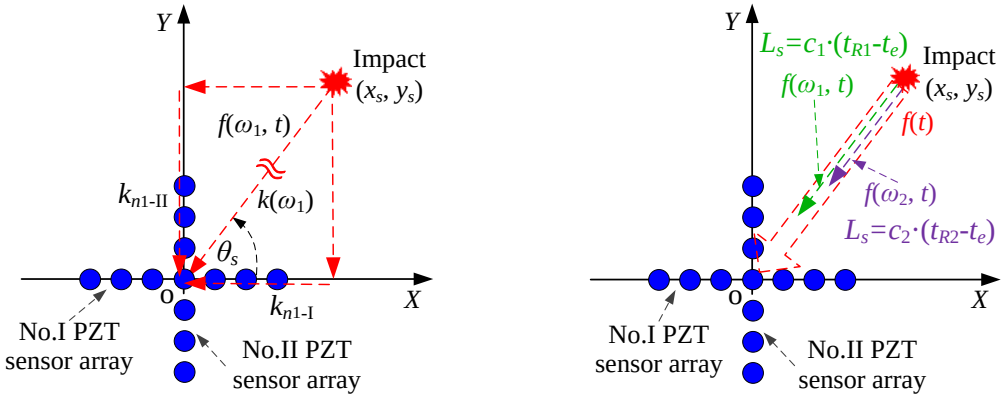

(a) Impact direction estimation (b) Impact distance calculation

Fig. 4. Schematic diagram of impact localization based on the 2D cross-shaped array

When the impact response signals of the two linear PZT sensor arrays are acquired, the frequency narrowband signals of central frequency ω_1 and central frequency ω_2 can be extracted respectively. ω_1 is set to be higher than ω_2. For the frequency narrowband signal of central frequency ω_1, the best-match wavenumbers and the arrival times, ($k_{n1\text{-I}}$, $t_{R1\text{-I}}$) and ($k_{n1\text{-II}}$, $t_{R1\text{-II}}$), can be obtained by using the impact imaging method. The same can be also done for the frequency narrowband signal of central frequency ω_2, and best-match wavenumbers and the arrival times, ($k_{n2\text{-I}}$, $t_{R2\text{-I}}$) and ($k_{n2\text{-II}}$, $t_{R2\text{-II}}$), can be also obtained. After that, the impact can be localized by using the following methods.

3.1. Impact direction estimation

As shown in Fig. 4(a), the wavenumber $k_{n1\text{-I}}$ can be seen as the X-axis projection wavenumber of $k(\omega_1)$ and the wavenumber $k_{n1\text{-II}}$ can be also seen as the Y-axis projection wavenumber of $k(\omega_1)$. They are expressed as Eq. (20).

$$k_{n1-\mathrm{I}} = k(\omega_1) \cdot \cos\theta_s \tag{20a}$$

$$k_{n1-\mathrm{II}} = k(\omega_1) \cdot \sin\theta_s \tag{20b}$$

Based on Eq. (20) and Eq. (21), the impact direction θ_s relative to the central point of the 2D cross-shaped array can be calculated in the range of [0°, 360°] without blind angle.

$$\theta_s = \begin{cases} \arctan(\dfrac{k_{n1-\mathrm{II}}}{k_{n1-\mathrm{I}}}) & (k_{n1-\mathrm{I}} > 0, k_{n1-\mathrm{II}} \geq 0) \\ 90^\circ & (k_{n1-\mathrm{I}} = 0, k_{n1-\mathrm{II}} > 0) \\ 180^\circ + \arctan(\dfrac{k_{n1-\mathrm{II}}}{k_{n1-\mathrm{I}}}) & (k_{n1-\mathrm{I}} < 0) \\ 270^\circ & (k_{n1-\mathrm{I}} = 0, k_{n1-\mathrm{II}} < 0) \\ 360^\circ + \arctan(\dfrac{k_{n1-\mathrm{II}}}{k_{n1-\mathrm{I}}}) & (k_{n1-\mathrm{I}} < 0, k_{n1-\mathrm{II}} > 0) \end{cases} \tag{21}$$

In actual situation of impact monitoring for composite structure, the wavenumber of the impact signal is dependent on the position of the impact. It means that the wavenumbers of the impact signals introduced by two impacts at different directions may have the same *X*-axis projection wavenumber. But this problem can be overcome by using the ratio between the *X*-axis projection wavenumber and *Y*-axis projection wavenumber, as shown in Eq. (21).

3.2. Impact distance calculation

As shown in Fig. 4(b), $t_{R1\text{-I}}$, $t_{R1\text{-II}}$, $t_{R2\text{-I}}$ and $t_{R2\text{-II}}$ are used to calculate the impact distance based on the group velocity difference between the frequency narrowband signals of two different central frequencies. The group velocities of the two frequencies are denoted as c_1 and c_2 respectively. c_1 is corresponding to the frequency narrowband signal of higher frequency ω_1, and c_2 is corresponding to the frequency narrowband signal of lower frequency ω_2. The impact distance relative to the two linear PZT sensor array can be calculated based on Eq. (22):

$$L_{s-j} = c_1 \cdot (t_{R1-j} - t_e) \tag{22a}$$

$$L_{s-j} = c_2 \cdot (t_{R2-j} - t_e) \tag{22b}$$

Where t_e is the impact occurrence time, j=I, II.

The impact distance L_s relative to the central point of the 2D cross-shaped array can be obtained based on Eq. (23).

$$L_{s-\mathrm{I}} = \frac{(t_{R2-\mathrm{I}} - t_{R1-\mathrm{I}})c_1 c_2}{c_1 - c_2} \tag{23a}$$

$$L_{s-\mathrm{II}} = \frac{(t_{R2-\mathrm{II}} - t_{R1-\mathrm{II}})c_1 c_2}{c_1 - c_2} \tag{23b}$$

$$L_s = \frac{L_{s-\mathrm{I}} + L_{s-\mathrm{II}}}{2} \tag{23c}$$

It should be noted that the error of distance calculation is dependent on the arrival time difference between the two frequencies. For example, the distance calculation result obtained by using No.I PZT array can be expressed as Eq. (23a). If there is a time error denoted as t_{error} in the arrival time estimation results, the distance calculation result can be expressed as Eq. (24). Thus, the distance calculation error can be expressed as Eq. (25). It indicates that if the arrival time difference between the two frequencies is larger, the distance calculation error will be smaller.

$$L'_{s-\mathrm{I}} = \frac{\left[\left(t_{R2-\mathrm{I}} - t_{R1-\mathrm{I}}\right) + t_{error}\right] \cdot c_1 c_2}{c_1 - c_2} \tag{24}$$

$$Error_L = \frac{L'_{s-\mathrm{I}} - L_{s-\mathrm{I}}}{L_{s-\mathrm{I}}} \times 100\% = \frac{t_{error}}{t_{R2-\mathrm{I}} - t_{R1-\mathrm{I}}} \times 100\% \tag{25}$$

Based on the direction and distance estimation results, the final impact position can be obtained by using Eq. (26):

$$x_s = L_s \cdot \cos\theta_s \tag{26a}$$

$$y_s = L_s \cdot \sin\theta_s \tag{26b}$$

4. Validation experiment on a carbon fiber composite laminate plate

4.1. Experimental setup

The experimental system shown in Fig. 5 is constructed by a carbon fiber composite laminate plate, a 2D cross-shaped array, an integrated SHM system and an impact hammer. The composite plate is made of T300/QY8911 carbon fiber and the dimension is 600 mm×600 mm×2.25 mm (length × width × thickness). It consists of 18 stacked layers and the ply sequence is $[45/0/-45/90/0/-45/0/-45/0]_s$. The thickness of each layer is 0.125 mm. The material property of each layer is given in Table 1.

Each linear PZT sensor array of the 2D cross-shaped array is constructed by 7 PZT-5A sensors. The diameter and thickness of the PZT sensors are 8 mm and 0.48 mm respectively. The distance between the centers of each two adjacent PZT sensors is Δx=10.0 mm. According to Eq. (13), the maximum cutoff wavenumber of the linear PZT sensor array is $k_{\max}$=314 rad/m. The PZT sensors in the array No.I are labeled as PZT I-1, PZT I-2 … PZT I-7, while those in the array No.II are labeled as PZT II-1, PZT II-2 … PZT II-7.

Another 3 reference PZT sensors are used to measure the group velocity, and their positions labeled as Ref 1, Ref 2 and Ref 3 are shown in Fig. 5(c) and Table 2.

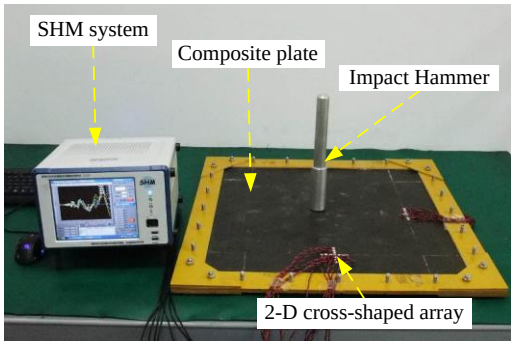

(a) Experimental setup

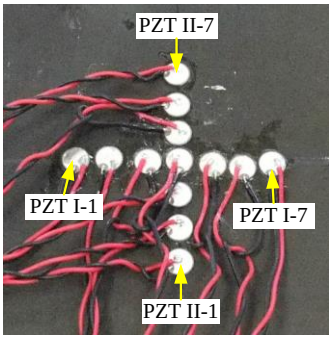

(b) The 2D cross-shaped array

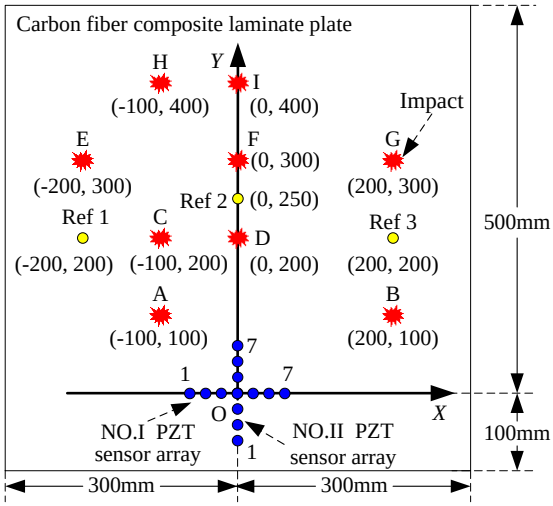

(c) The impact positions and the placement of the 2D cross-shaped array

Fig. 5. Illustration of the validation experiment performed on the composite plate

Table 1. The material property of a single layer of the composite plate

Parameter	Value
0º tensile modulus (GPa)	135
90º tensile modulus (GPa)	8.8
±45º in-plane shearing modulus (GPa)	4.47
Poisson ratio μ	0.328
Density (kg·m^{-3})	1.61×10^3

The impact hammer is used to apply the impact of 2J energy to the plate. 9 impacts labeled as A to I are performed at various positions on the composite plate, as shown in Fig. 5(c) and Table 2. The impact direction is defined according to the counterclockwise direction relative to *X*-axis positive direction.

The integrated SHM system developed by the authors [37] is adopted to acquire the impact response signals. The sampling rate is 10 MS/s. The sampling length is 10000 samples including 6000 pre-trigger samples. The trigger voltage is set to be 1 V.

Table 2. The positions of the impacts and the reference PZT sensors on the composite plate

Position label	Cartesian coordinates (mm, mm)	Polar coordinates (°, mm)
Ref 1	(-200, 200)	(135.0, 282.8)
Ref 2	(0, 250)	(90.0, 250.0)
Ref 3	(200, 200)	(45.0, 282.8)
A	(-100, 100)	(135.0, 141.4)
B	(200, 100)	(26.6, 223.6)
C	(-100, 200)	(116.6, 223.6)
D	(0, 200)	(90.0, 200.0)
E	(-200, 300)	(123.7, 360.6)
F	(0, 300)	(90.0, 300.0)
G	(200, 300)	(56.3, 360.6)
H	(-100, 400)	(104.0, 412.3)
I	(0, 400)	(90.0, 400.0)

4.2. Frequency selection

A typical impact response signal of the impact G, which is acquired by using PZT I-1, is shown in Fig. 6(a). It can be seen from the frequency spectrum shown in Fig. 6(b) that the frequency range of the impact response signal is mainly in 0~50 kHz approximately.

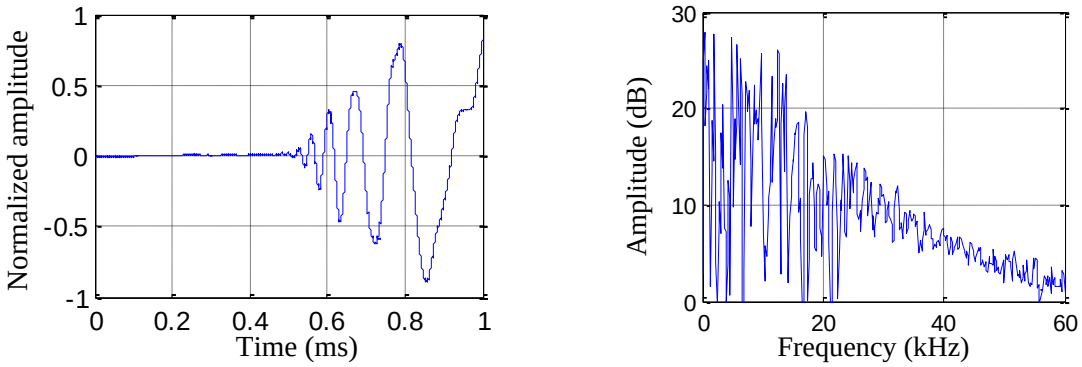

(a) Impact response signal (b) Frequency spectrum

Fig. 6. A typical impact response signal and its frequency spectrum on the composite plate

As mentioned in Section 2 and Section 3, the frequency narrowband signals of two different central frequencies are needed to be extracted from the frequency wideband impact response signals to realize impact imaging and localization.

For the frequency narrowband signal of higher central frequency, the frequency selection should consider the following three points. (1) The selected frequency should be in the range of 0~50 kHz

considering the energy of the impact response signal. (2) The selected frequency should be high to reduce the wavenumber match error because the actual wavenumber is bigger the wavenumber match error is smaller. (3) The *X*-axis projection wavenumber of the frequency narrowband signal or the *Y*-axis projection wavenumber should be smaller than the maximum cutoff wavenumber. Considering the three points, the higher frequency is selected to be 40 kHz. The extracted frequency narrowband signal and the corresponding frequency spectrum are shown in Fig. 7.

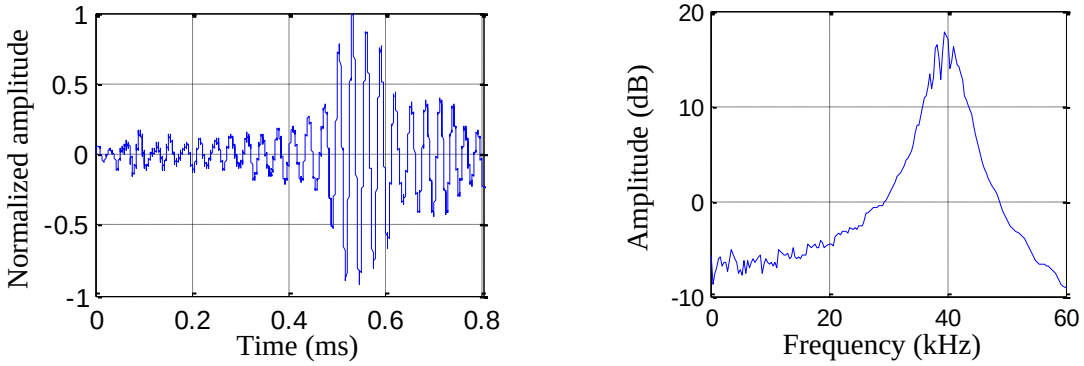

(a) Frequency narrowband signal (b) Frequency spectrum

Fig. 7. The frequency narrowband signal of 40 kHz on the composite plate

For the frequency narrowband signal of lower central frequency, the difference between the higher frequency and the lower frequency should be set to be larger to reduce the distance calculation error, which is discussed in Section 3.2 and shown in Eq. (26). But if the frequency is too low, the time domain resolution will be too much low to determine the arrival time. Thus, the lower frequency is selected to be 20 kHz. The extracted frequency narrowband signal and the corresponding frequency spectrum are shown in Fig. 8.

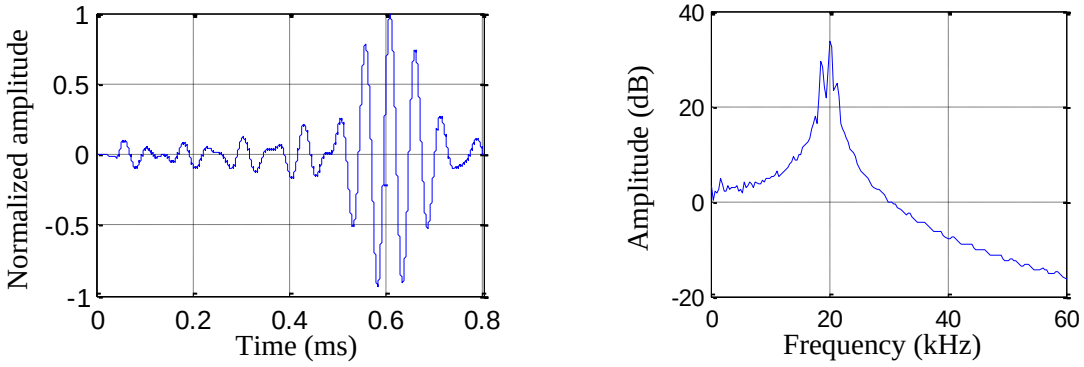

(a) Frequency narrowband signal (b) Frequency spectrum

Fig. 8. The frequency narrowband signal of 20 kHz on the composite plate

4.3. Group velocity measuring

In this paper, the group velocity measuring method proposed in the reference [22] is used to measure the group velocity of the frequency narrowband signal. The modulated five-cycle sine burst signal is used to be the frequency narrowband excitation signal. The frequency range of the excitation signal is swept from 20 kHz to 60 kHz with an interval of 5 kHz.

The process of the group velocity measuring is described as follows. 1) The excitation signal is input to PZT sensor Ref 1 to excite frequency narrowband signal propagating on the composite plate. 2) The corresponding frequency narrowband response signals of all the 13 PZT sensors in the 2D cross-shaped array are acquired. 3) For each PZT sensor, a group velocity can be obtained. 4) The average group velocity is obtained by averaging the 13 group velocities obtained by using the 13 PZT sensors, as shown in Fig. 9(a). Based on the same process, the measured average group velocity by using PZT sensor Ref 2 and Ref 3 are shown in Fig. 9(b) and (c) respectively. Finally, the whole average group velocity c_1 =1461.06 m/s and c_2 =1152.60 m/s corresponding to the two frequencies 40 kHz and 20 kHz are obtained.

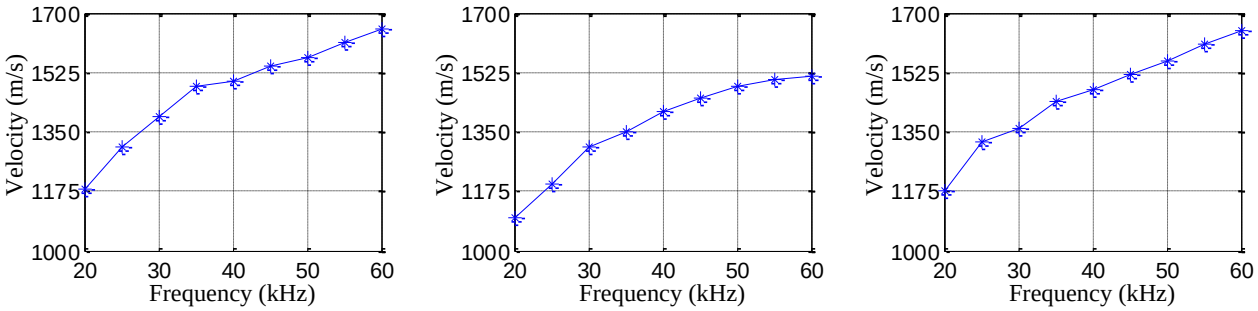

(a) The measured group velocity (Ref 1) (b) The measured group velocity (Ref 2) (c) The measured group velocity (Ref 3)

Fig. 9. The measured group velocities on the composite plate by using the 3 reference PZT sensors

4.4. Impact imaging results and discussion

4.4.1. Impact imaging process and the results

In this paper, the impact G is chosen to be an example to show the impact imaging and localization process. The waterfall plot of the frequency wideband impact response signals of the 2D cross-shaped array are shown in Fig. 10. The frequency narrowband signals of 40 kHz and 20 kHz are extracted from the frequency wideband impact response signals respectively, and their plots are shown in Fig. 11 and Fig. 12 respectively.

The model-independent spatial-wavenumber filter based impact imaging method is applied to the frequency narrowband signals to obtain the wavenumber-time images, as shown in Fig. 13 and Fig. 14. The wavenumber searching range is set to be [-314 rad/m, 314 rad/m] and the wavenumber searching interval is

set to be Δk=1 rad/m.

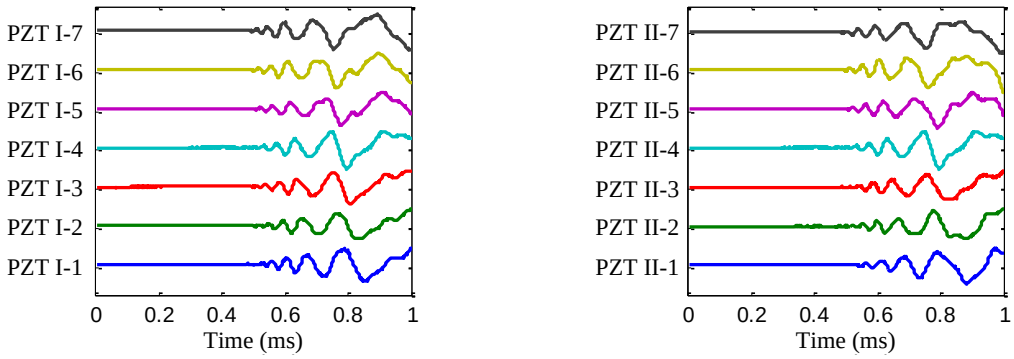

(a) Impact response signals of No.I array (b) Impact response signals of No.II array

Fig. 10. The frequency wideband impact response signals of the impact G on the composite plate

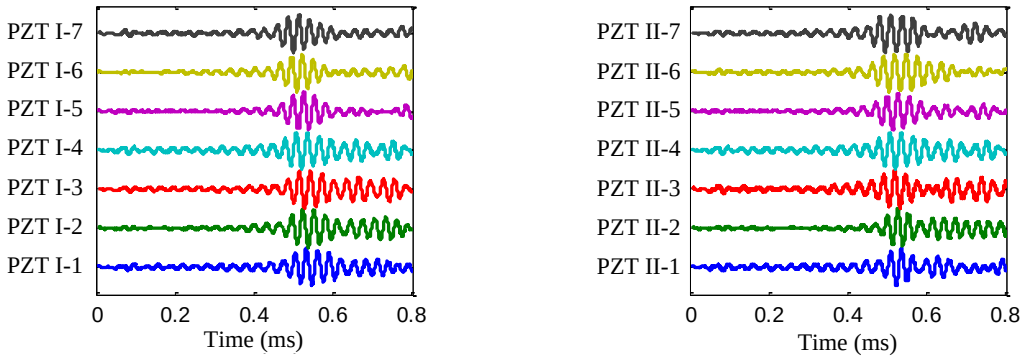

(a) Frequency narrowband signals of No.I array (b) Frequency narrowband signals of No.II array

Fig. 11. The frequency narrowband signals of 40 kHz of the impact G on the composite plate

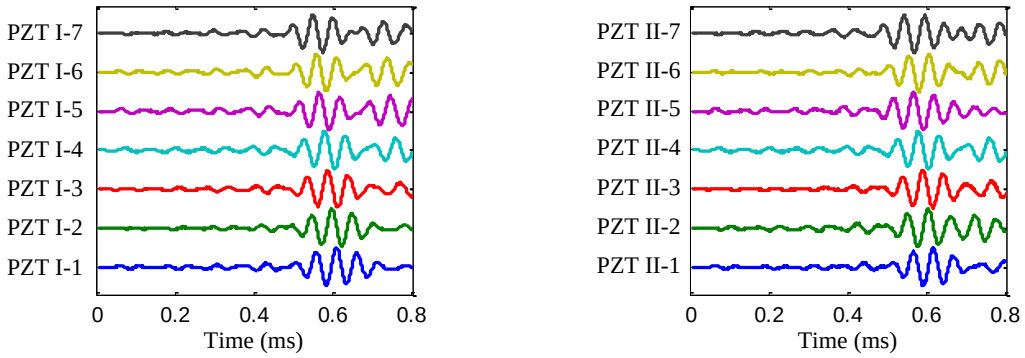

(a) Frequency narrowband signals of No.I array (b) Frequency narrowband signals of No.II array

Fig. 12. The frequency narrowband signals of 20 kHz of the impact G on the composite plate

In the wavenumber-time images, the pixel values of all the image points are normalized. For the frequency narrowband signals of 40 kHz, the best-match wavenumbers and the arrival times ($k_{n1\text{-I}}$=161 rad/m and $k_{n1\text{-II}}$=229 rad/m, $t_{R1\text{-I}}$=0.5192 ms and $t_{R1\text{-II}}$=0.5193 ms) are obtained. Based on Eq. (21), the impact direction θ_s=54.9° of the impact G relative to the 2D cross-shaped array can be obtained. For the frequency narrowband signals of 20 kHz, the impact arrival times ($t_{R2\text{-I}}$=0.5819 ms and $t_{R2\text{-II}}$=0.5872 ms) can be

obtained. Based on Eq. (23), the impact distance L_s=356.5 mm can be obtained. Finally, the impact position (x_s, y_s) is obtained to be (205.0 mm, 291.6mm) based on Eq. (26). The impact localization error is 9.8 mm.

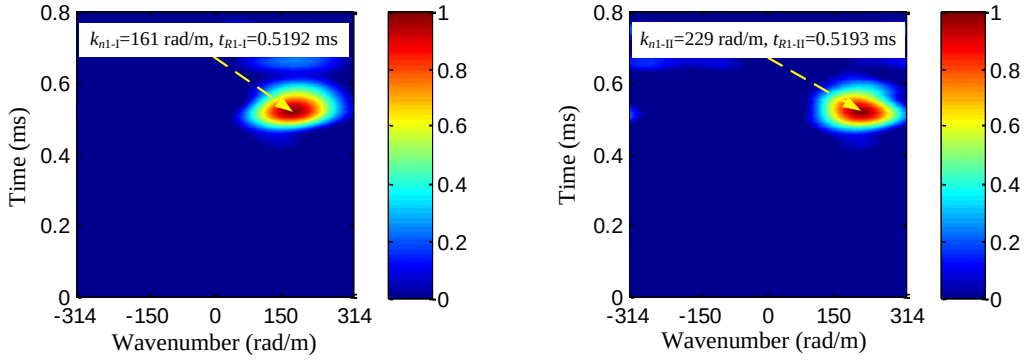

(a) Impact imaging result of No.I array (b) Impact imaging result of No.II array

Fig. 13. Impact imaging results of the composite plate (Impact G, 40 kHz)

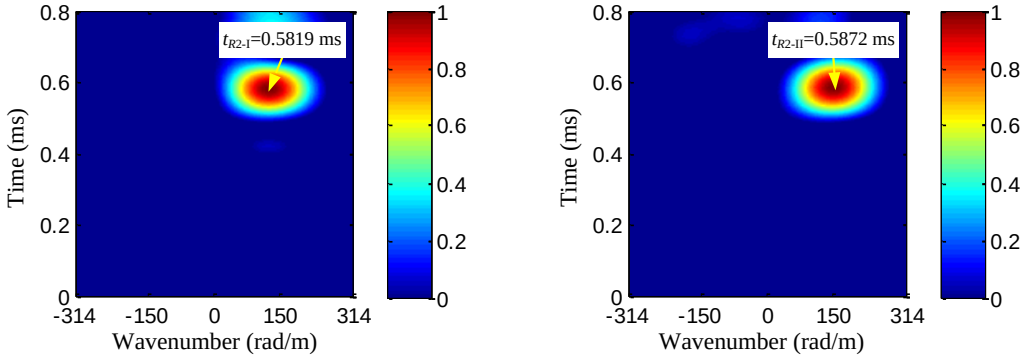

(a) Impact imaging result of No.I array (b) Impact imaging result of No.II array

Fig. 14. Impact imaging results of the composite plate (Impact G, 20 kHz)

Table 3. Impact localization results of the 9 impacts applied on the composite plate

Impact label	($k_{n1\text{-I}}$, $t_{R1\text{-I}}$) (rad/m, ms)	($k_{n2\text{-II}}$, $t_{R1\text{-II}}$) (rad/m, ms)	$t_{R2\text{-I}}$ (ms)	$t_{R2\text{-II}}$ (ms)	Localized position (°, mm)	Actual position (°, mm)	Direction and distance error (°, mm)	Localization error (mm)
A	(-205, 0.5275)	(191, 0.5268)	0.5539	0.5551	(137.0, 149.3)	(135.0, 141.4)	(2.0, 7.9)	9.4
B	(268, 0.4829)	(124, 0.4838)	0.5317	0.5170	(24.8, 223.8)	(26.6, 223.6)	(-1.8, 0.2)	6.8
C	(-137, 0.5489)	(261, 0.5478)	0.5917	0.5879	(117.7, 226.3)	(116.6, 223.6)	(1.1, 2.7)	5.2
D	(5, 0.5758)	(281, 0.5762)	0.6124	0.6153	(89.0, 206.6)	(90.0, 200.0)	(-1.0, 6.6)	7.6
E	(-168, 0.2897)	(240, 0.2870)	0.3635	0.3463	(125.0, 363.3)	(123.7, 360.6)	(1.3, 2.7)	8.7
F	(7, 0.4180)	(280, 0.4199)	0.4738	0.4751	(88.6, 303.0)	(90.0, 300.0)	(-1.4, 3.0)	8.1
G	(161, 0.5192)	(229, 0.5193)	0.5819	0.5872	(54.9, 356.5)	(56.3, 360.6)	(-1.4, -4.1)	9.8
H	(-71, 0.4952)	(273, 0.4961)	0.5699	0.5698	(104.6, 405.1)	(104.0, 412.3)	(0.6, -7.2)	8.2
I	(5, 0.4066)	(278, 0.4076)	0.4771	0.4817	(89.0, 394.7)	(90.0, 400.0)	(-1.0, -5.3)	8.9

According to the process described above, the impact localization results of the impacts applied to the other positions can be also obtained, as shown in Table 3. The results indicate that the error of the impact direction estimation is no more than 2° and the error of the impact distance estimation is less than 10 mm. The maximum impact localization error is no more than 10 mm on the composite plate in the monitoring range of

500 mm×500 mm.

4.4.2. Impact localization error caused by the error of PZT sensors placement

The impact localization results shown in Table 3 are obtained by supposing that the PZT sensors of the 2D cross-shaped array are placed accurately. In other words, the 2D cross-shaped array is supposed to be a 2D cross-shaped uniform array and the placement error of the PZT sensors is not taken into consideration. In order to study the relationship between the precision of PZT sensor placement and the impact localization error, a series of 2D cross-shaped non-uniform arrays are simulated as listed in Table 4. The error range of the PZT sensors placement is set to be [-1 mm, +1 mm] because the distance between the edges of each two adjacent PZT sensors is 2 mm in the uniform array.

Based on these 2D cross-shaped non-uniform arrays, the localization results of the impact G is shown in Table 5. The maximum impact localization error is also no more than 10 mm and the average impact localization error is 7.6 mm. It means that the influence of the PZT sensors placement error on the new proposed method is low.

Table 4. The coordinate of the PZT sensors of the 2D cross-shaped non-uniform arrays

	No.I array (x_m, 0) (mm)	No.II array (0, y_m) (mm)
Uniform array	x_m = [-30.0, -20.0, -10.0, 0.0, 10.0, 20.0, 30.0]	y_m = [-30.0, -20.0, -10.0, 0.0, 10.0, 20.0, 30.0]
Non-uniform array 1	x_m = [-29.3, -19.8, -10.3, 0.0, 9.8, 19.2, 29.5]	y_m = [-30.8, -20.6, -10.5, -0.2, 9.1, 20.8, 30.9]
Non-uniform array 2	x_m = [-30.0, -20.0, -10.3, 0.8, 9.7, 19.2, 30.6]	y_m = [-30.2, -20.5, -10.2, -0.8, 9.3, 20.9, 30.9]
Non-uniform array 3	x_m = [-29.8, -20.9, -10.5, -0.3, 10.6, 19.0, 29.1]	y_m = [-30.7, -19.7, -9.5, 0.3, 9.9, 20.1, 29.6]
Non-uniform array 4	x_m = [-29.5, -20.6, -9.6, -0.6, 9.7, 20.3, 30.6]	y_m = [-30.8, -19.1, -9.4, 0.0, 9.9, 19.9, 29.6]
Non-uniform array 5	x_m = [-30.0, -20.0, -9.4, 0.6, 10.3, 19.8, 30.6]	y_m = [-29.9, -20.3, -9.1, 0.8, 10.1, 20.2, 30.2]

Table 5. The localization results of the impact G by using the 2D cross-shaped non-uniform arrays

	($k_{n1\text{-I}}$, $t_{R1\text{-I}}$) (rad/m, ms)	($k_{n1\text{-II}}$, $t_{R1\text{-II}}$) (rad/m, ms)	$t_{R2\text{-I}}$ (ms)	$t_{R2\text{-II}}$ (ms)	Localized position (°, mm)	Direction and Distance error (°, mm)	Localization error (mm)
Uniform array	(161, 0.5192)	(229, 0.5193)	0.5819	0.5872	(54.9, 356.5)	(-1.4, -4.1)	9.8
Non-uniform array 1	(163, 0.5192)	(235, 0.5193)	0.5819	0.5872	(55.3, 356.5)	(-1.0, -4.1)	7.7
Non-uniform array 2	(155, 0.5192)	(227, 0.5193)	0.5819	0.5872	(55.7, 356.5)	(-0.6, -4.1)	5.7
Non-uniform array 3	(159, 0.5192)	(231, 0.5193)	0.5819	0.5872	(55.5, 356.5)	(-0.8, -4.1)	6.7
Non-uniform array 4	(160, 0.5192)	(233, 0.5193)	0.5819	0.5864	(55.5, 354.3)	(-0.8, -6.3)	7.9
Non-uniform array 5	(162, 0.5192)	(230, 0.5193)	0.5819	0.5872	(54.8, 356.5)	(-1.5, -4.1)	10.0

5. Validation of the impact imaging method on an aircraft composite oil tank

5.1. Validation setup

The validation system shown in Fig. 17 is constructed by an aircraft composite oil tank, a 2D cross-shaped array, the integrated SHM system and the impact hammer. The dimension of the oil tank is

600mm×300mm×240mm (length×width×height).

The composite panel of the oil tank is made of T300/QY8911 carbon fiber and it is thickness variable, as shown in Fig. 18. The central part is the thickest part and consists of 58 stacked layers. The ply sequence is $[45/0/-45/0/90/0/45/0/-45/0/45/0_2/45/0/-45/0/-45/0_2/45/0/90/0/-45/0/45/0/-45]_s$. The thickness of each layer is 0.125 mm and the total thickness is 7.25 mm. The thinnest parts of the panel are at the two ends and the thicknesses are both 4.5 mm. The material property of each layer is the same as the composite plate described in Section 4.1.

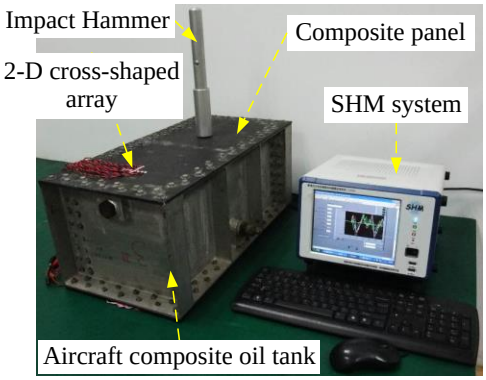

(a) Validation system

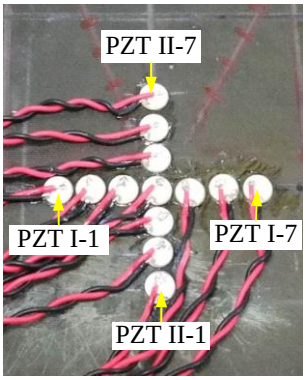

(b) The 2D cross-shaped array

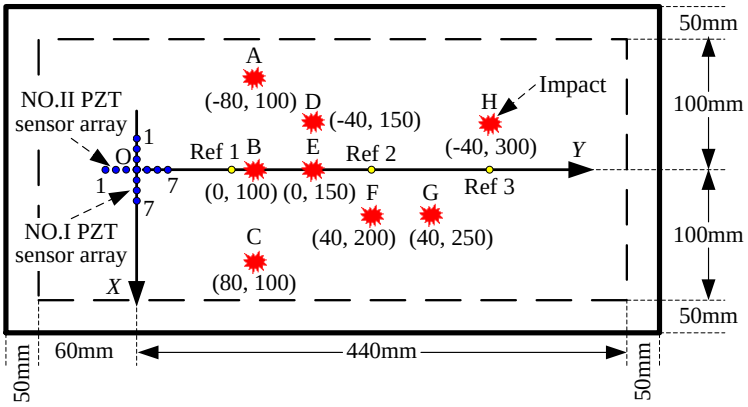

(c) The impact positions and the placement of the 2D cross-shaped array

Fig. 17. Illustration of the validation experiment performed on the composite oil tank

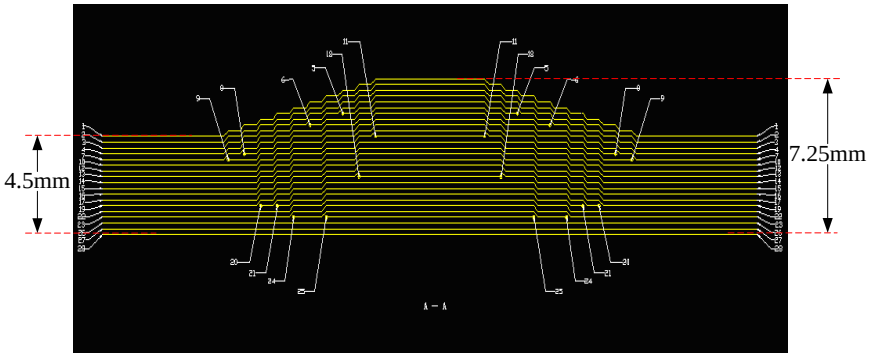

Fig. 18. Variable thickness illustration of the composite panel of the oil tank

As shown in Fig. 17(b), each linear PZT sensor array of the 2D cross-shaped array is constructed by 7 PZT-5A sensors. The diameter and thickness of the PZT sensors are also 8 mm and 0.48 mm respectively. The distance between the centers of each two adjacent PZT sensors is Δx=9.0 mm. According to Eq. (17), the maximum cutoff wavenumber of the linear PZT sensor array is $k_{max} \approx 349$ rad/m. Another 3 reference PZT sensors are used to measure the group velocity, and their positions labeled as Ref 1, Ref 2 and Ref 3 are shown in Fig. 17(c) and Table 6.

The impact hammer is used to apply the impact of 2J energy to the composite oil tank. 8 impacts labeled as A to I are performed at various positions on the composite panel, as shown in Fig. 17(c) and Table 6.

Table 6. The positions of the impacts and the reference PZT sensors on the composite oil tank

Position label	Cartesian coordinates (mm, mm)	Polar coordinates (°, mm)
Ref 1	(0, 80)	(90.0, 80.0)
Ref 2	(0, 200)	(90.0, 200.0)
Ref 3	(0, 300)	(90.0, 300.0)
A	(-80, 100)	(128.7, 128.1)
B	(0, 100)	(90.0, 100.0)
C	(80, 100)	(51.3, 128.1)
D	(-40, 150)	(104.9, 155.2)
E	(0, 150)	(90.0, 150.0)
F	(40, 200)	(78.7, 204.0)
G	(40, 250)	(80.9, 253.2)
H	(-40, 300)	(97.6, 302.7)

5.2. Frequency selection and group velocity measuring

A typical impact response signal of the impact D, which is acquired by PZT I-1, is shown in Fig. 19(a). It can be seen from the frequency spectrum shown in Fig. 19(b) that the frequency range of the impact response signal is also mainly in 0~50 kHz approximately.

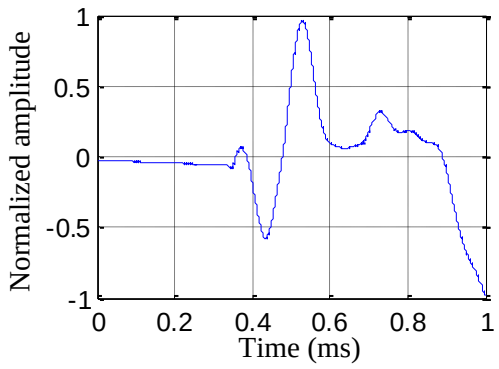

(a) Impact response signal

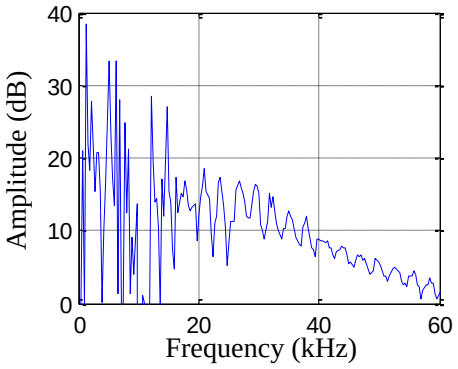

(b) Frequency spectrum

Fig. 19. A typical impact response signal and its frequency spectrum on the composite oil tank

Based on the frequency selection discussion in Section 4.2, the higher frequency is selected to be 50 kHz and the lower frequency is selected to be 20 kHz. The extracted frequency narrowband signals of the two frequencies are shown in Fig. 20 and Fig. 21 respectively.

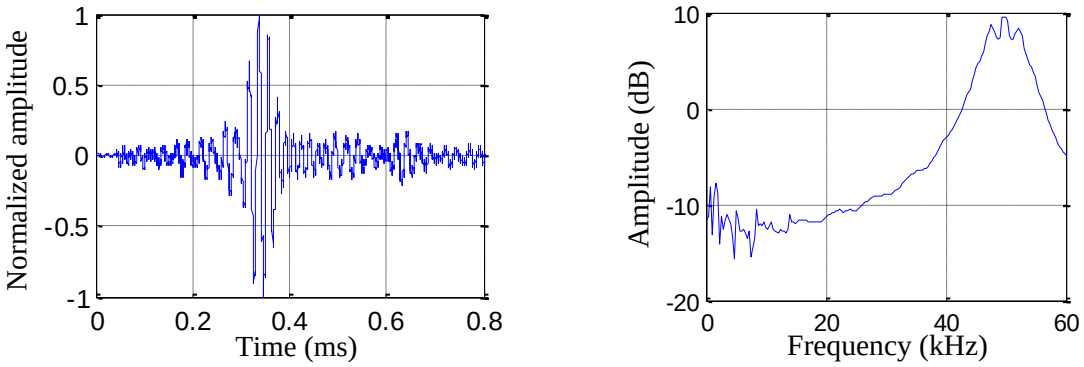

(a) Frequency narrowband signal (b) Frequency spectrum

Fig. 20. The frequency narrowband signal of 50 kHz on the composite oil tank

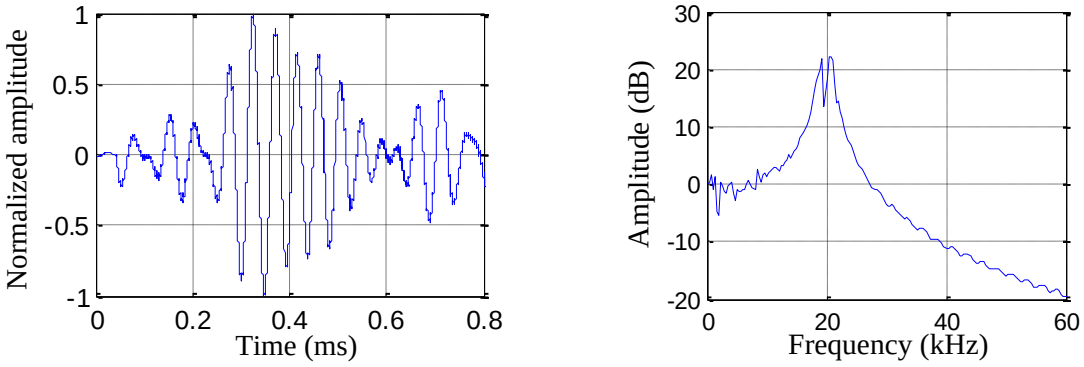

(a) Frequency narrowband signal (b) Frequency spectrum

Fig. 21. The frequency narrowband signal of 20 kHz on the composite oil tank

As discussed in Section 4.3, the measured group velocity of each frequency on the composite oil tank by using the 3 reference PZT sensors is shown in Fig. 22. The whole average group velocity c_1=1811.05 m/s and c_2=1199.91 m/s corresponding to the two frequencies 50 kHz and 20 kHz are obtained.

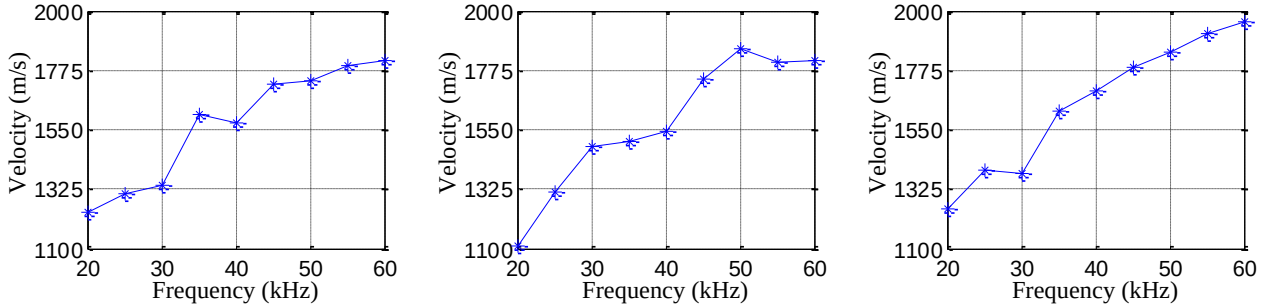

(a) The measured group velocity (Ref 1) (b) The measured group velocity (Ref 2) (c) The measured group velocity (Ref 3)

Fig. 22. The measured group velocities on the composite oil tank by using the 3 reference PZT sensors

5.3. Impact imaging results and discussion

The impact D is selected to be an example to discuss the impact imaging and localization result. The waterfall plots of the frequency wideband impact response signals of the 2D cross-shaped array are shown in Fig. 23.

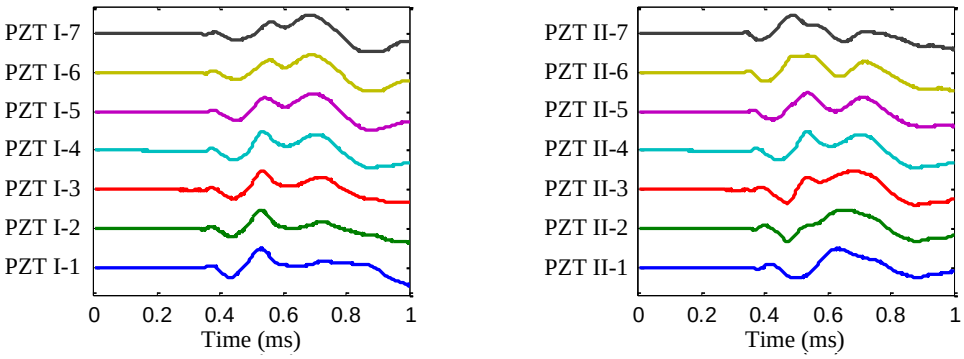

(a) Impact response signals of No.I array (b) Impact response signals of No.II array

Fig. 23. The frequency wideband impact response signals of the impact D on the composite oil tank

The frequency narrowband signals of 50 kHz and 20 kHz are extracted from the frequency wideband impact response signals respectively, and their plots are shown in Fig. 24 and Fig. 25 respectively.

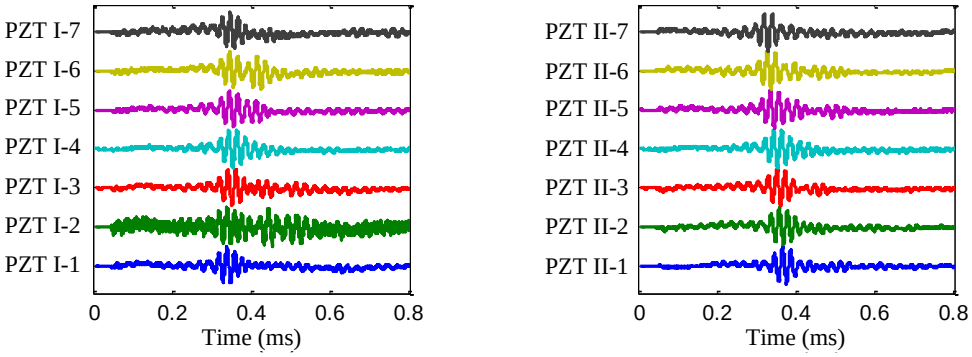

(a) Frequency narrowband signals of No.I array (b) Frequency narrowband signals of No.II array

Fig. 24. The frequency narrowband signals of 50 kHz of the impact D on the composite oil tank

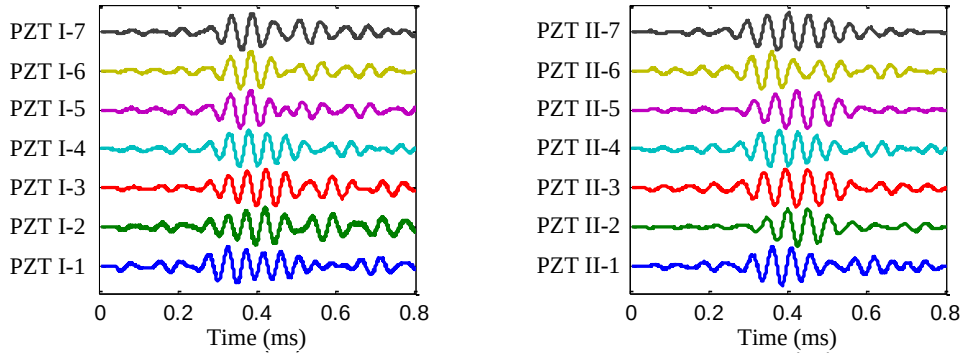

(a) Frequency narrowband signals of No.I array (b) Frequency narrowband signals of No.II array

Fig. 25. The frequency narrowband signals of 20 kHz of the impact D on the composite oil tank

The model-independent spatial-wavenumber filter based impact imaging method is applied to the frequency narrowband signals to obtain the wavenumber-time images, as shown in Fig. 26 and Fig. 27. The wavenumber searching range is set to be [-349 rad/m, 349 rad/m] and the wavenumber searching interval is set to be Δk=1 rad/m. For the frequency narrowband signals of 50 kHz, the best-match wavenumbers and the arrival times ($k_{n1\text{-I}}$=-64 rad/m and $k_{n1\text{-II}}$=261 rad/m, $t_{R1\text{-I}}$=0.3468 ms and $t_{R1\text{-II}}$=0.3487 ms) are obtained. Based on Eq. (21), the impact direction θ_s=103.8° of the impact D relative to the 2D cross-shaped array can be obtained. For the frequency narrowband signals of 20 kHz, the impact arrival times ($t_{R2\text{-I}}$=0.3891 ms and $t_{R2\text{-II}}$=0.3848 ms) can be obtained. Based on Eq. (23), the impact distance L_s=139.4 mm can be obtained. Finally, the impact position is obtained to be (-33.2 mm, 135.4 mm) based on Eq. (26). The impact localization error is 16.1 mm.

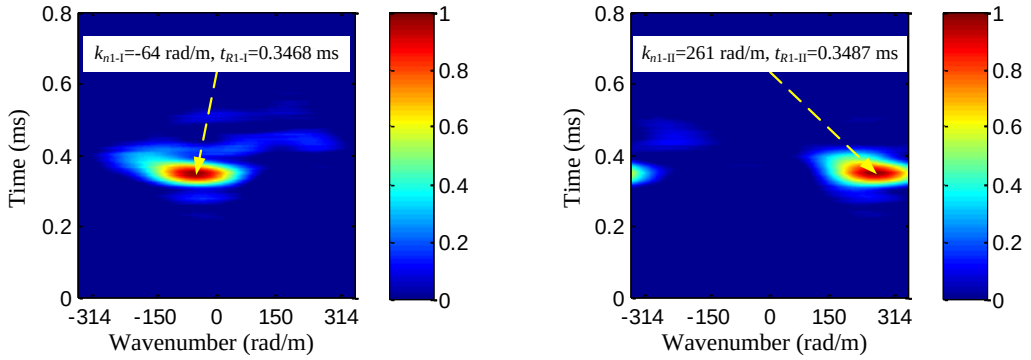

(a) Impact imaging result of No.I array (b) Impact imaging result of No.II array

Fig.26. Impact imaging results of the composite oil tank (Impact D, 50 kHz)

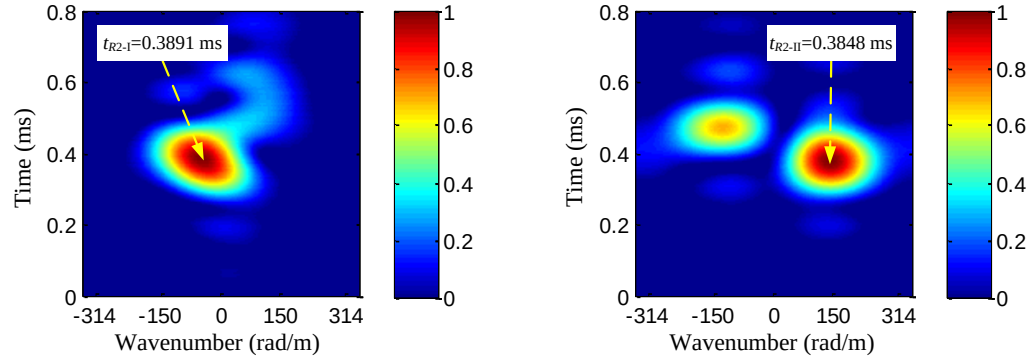

(a) Impact imaging result of No.I array (b) Impact imaging result of No.II array

Fig.27. Impact imaging results of the composite oil tank (Impact D, 20 kHz)

The summary of the impact localization results of the 8 impacts is listed in Table 7. For the impact A, B, C, D and E, the error of the impact direction estimation is less than 3° and the error of the impact distance estimation is less than 20 mm. For the impact F, G and H, the error of the impact direction estimation is also

less than 3° but the error of the impact distance estimation is larger than 20 mm. It is mainly caused by the group velocity error introduced by the variable thickness structural part.

Table 7. Impact localization results of the 8 impacts applied to the composite oil tank

Impact label	($k_{n1\text{-I}}$, $t_{R1\text{-I}}$) (rad/m, ms)	($k_{n2\text{-II}}$, $t_{R1\text{-II}}$) (rad/m, ms)	$t_{R2\text{-I}}$ (ms)	$t_{R2\text{-II}}$ (ms)	Localized position (°, mm)	Actual position (°, mm)	Direction and distance error (°, mm)	Localization error (mm)
A	(-155, 0.4746)	(210, 0.4824)	0.5114	0.5184	(126.4, 129.4)	(128.7, 128.1)	(-2.3, 1.3)	5.2
B	(2, 0.4652)	(275, 0.4668)	0.4856	0.4965	(89.6, 89.1)	(90.0, 100.0)	(-0.4, -10.9)	10.9
C	(152, 0.4101)	(209, 0.4125)	0.4369	0.4469	(54.0, 108.8)	(51.3, 128.1)	(2.7, -19.3)	20.0
D	(-64, 0.3468)	(261, 0.3487)	0.3891	0.3848	(103.8, 139.4)	(104.9, 155.2)	(-1.1, -15.8)	16.1
E	(-6, 0.3261)	(272, 0.3256)	0.3664	0.3600	(91.3, 132.8)	(90.0, 150.0)	(1.3, -17.2)	17.5
F	(45, 0.2099)	(275, 0.2071)	0.2582	0.2613	(80.7, 182.2)	(78.7, 204.0)	(2.0, -21.8)	22.8
G	(48, 0.4681)	(256, 0.4667)	0.5226	0.5350	(79.4, 218.3)	(80.9, 253.2)	(-1.5, -34.9)	35.4
H	(-46, 0.4696)	(279, 0.4786)	0.5636	0.5763	(99.4, 340.8)	(97.6, 302.7)	(1.8, 38.1)	39.4

6. Conclusion

This paper proposes a new impact imaging and location method based on spatial-wavenumber filtering technique and dense PZT sensor array. With this method, the continuous complex Shannon wavelet transform is adopted to extract frequency narrowband signals from the frequency wideband impact response signals. A model-independent spatial filter is designed and a wavenumber searching and best match mechanism is proposed to fulfill the spatial-wavenumber filtering of the frequency narrowband signals without wavenumber measuring or modeling. Based on the model-independent spatial filter, a 2D cross-shaped array is adopted to realize the impact imaging and localization without blind angle. The impact monitoring feasibility of this method is validated on a carbon fiber composite laminate plate. The validation results show good impact localization accuracy, and the maximum localization error is less than 10 mm in the monitoring range of 500mm×500mm. This method is also validated on an aircraft thickness variable composite oil tank. The validation results show that the impact direction can be estimated accurately on the complex composite structure, but the accuracy of the impact distance estimation is limited by the error of the group velocity.

However, the theoretical fundamental of this method is based on far-field situation, which limits the performance of this method. In addition, this method is dependent on the group velocity, which further limits the performance. Thus, the ongoing work is to develop a model-independent spatial filter based impact imaging method which can be applied to full-field impact monitoring on complex composite structure and does not rely on the group velocity.

Acknowledgements

This work is supported by the National Science Fund for Distinguished Young Scholars (Grant No.51225502), the Natural Science Foundation of China (Grant No.51205189), the Chinese Foundation of Postdoctoral Science (Grant No.2012M510134), the Research Funds for the Doctoral Program of Higher Educations in China (Grant No.20123218120007), State Key Laboratory of Mechanics and Control of Mechanical Structures (Nanjing University of Aeronautics and Astronautics) (Grant No.MCMS-0513K01 and Grant No. 0515Y01), the Priority Academic Program Development of Jiangsu Higher Education Institutions and Qing Lan Project.

Reference

[1] W.J. Staszewski, S. Mahzan, R. Traynor, Health monitoring of aerospace composite structures-Active and passive approach, Compos. Sci. Technol. 69 (2009) 1678-1685.

[2] C. Boller, F.K. Chang, Y. Fujino, Encyclopedia of Structural Health Monitoring, John Wiley and Sons, Hoboken, 2009.

[3] M. Meo, G. Zumpano, M. Piggott, G. Marengo, Impact identification on a sandwich plate from wave propagation responses, Compos. Struct. 71 (2005) 302-306.

[4] T. Kundu, H. Nakatani, N. Takeda, Acoustic source localization in anisotropic plates, Ultrasonics 52 (2012) 740-746.

[5] J.R. LeClerc, K. Worden, W.J. Staszewski, J. Haywood, Impact detection in an aircraft composite panel-A neural-network approach, J. Sound Vib. 299 (2007) 672-682.

[6] J.F.C. Markmiller, F.K. Chang, Sensor network optimization for a passive sensing impact detection technique, Struct. Health Monit. 9 (2010) 25-39.

[7] C. Chen, F.G. Yuan, Impact source identification in finite isotropic plates using a time-reversal method: theoretical study, Smart Mater. Struct. 19 (2010) 105028.

[8] Z. Sharif-khodaei, M. Ghajari, M.H. Aliabadi, Determination of impact location on composite stiffened panel, Smart Mater. Struct. 21 (2012) 105026.

[9] C.H. Wang, T.J. Rose, F.K. Chang, A synthetic time-reversal imaging method for structural health monitoring, Smart Mater. Struct.13 (2004) 415-423.

[10] J.E. Michaels, Detection, localization and characterization of damage in plates with an in situ array of spatially distributed ultrasonic sensors, Smart Mater. Struct. 17 (2008) 035035.

[11] Z. Su, L. Cheng, X. Wang, L. Yu, C. Zhou, Predicting delamination of composite laminates using an imaging approach, Smart Mater. Struct. 18 (2009) 074002.

[12] L. Yu, V. Giurgiutiu, In situ 2-D piezoelectric wafer active sensors arrays for guided wave damage detection, Ultrasonics 48 (2008) 117-134.

[13] C. Holmes, B.W. Drinkwater, P.D. Wilcox, Advanced post-processing for scanned ultrasonic arrays: Application to defect detection and classification in non-destructive evaluation, Ultrasonics 48 (2008) 636-642.

[14] X.P. Qing, S. Beard, S.B. Shen, S. Banerjee, I. Bradley, M.M. Salama, F.K. Chang, Development of a real-time active pipeline integrity detection system, Smart Mater. Struct. 18 (2009) 115010.

[15] J.S. Hall, J.E. Michaels, Computational efficiency of ultrasonic guided wave imaging algorithms, IEEE Trans. Ultrason. Ferroelectr. Freq. Control 58 (2011) 244-248.

[16] C. Zhou, Z. Su, L. Cheng, Probability-based diagnostic imaging using hybrid features extracted from ultrasonic Lamb wave signals, Smart Mater. Struct. 20 (2011) 125005.

[17] T. Wandowski, P. Malinowski, W.M. Ostachowicz, Damage detection with concentrated configurations of piezoelectric transducers, Smart Mater. Struct. 20 (2011) 025002.

[18] L. Qiu, M. Liu, X. Qing, S. Yuan, A quantitative multidamage monitoring method for large-scale complex composite, Struct. Health Monit. 12 (2013) 183-196.

[19] R. Zhu, G.L. Huang, F.G. Yuan, Fast damage imaging using the time-reversal technique in the frequency-wavenumber domain, Smart Mater. Struct. 22 (2013) 075028.

[20] J. Park, S. Ha, F.K. Chang, Monitoring impact events using a system-identification method, AIAA J. 47 (2009) 2011-2021.

[21] F. Ciampa, M. Meo, Impact detection in anisotropic materials using a time reversal approach, Struct. Health Monit.11 (2012) 43-49.

[22] L. Qiu, S. Yuan, X. Zhang, Y. Wang, A time reversal focusing based impact imaging method and its evaluation on complex composite structures, Smart Mater. Struct. 20 (2011) 105014.

[23] Y. Zhong, S. Yuan, L. Qiu, Multiple damage detection on aircraft composite structures using near-field MUSIC algorithm, Sensor. Actuat. A-Phys. 214 (2014) 234-244.

[24] M. Ruzzene, Frequency-wavenumber domain filtering for improved damage visualization, Smart Mater. Struct. 16 (2007) 2116-2129.

[25] T.E. Michaels, J.E. Michaels, M. Ruzzene, Frequency-wavenumber domain analysis of guided

wavefields, Ultrasonics 51 (2011) 452-466.

[26] H. Sohn, D. Dutta, J.Y. Yang, M. DeSimio, S. Olson, E. Swenson, Automated detection of delamination and disbond from wavefield images obtained using a scanning laser vibrometer, Smart Mater. Struct. 20 (2011) 045017.

[27] L. Yu, C.A. Leckey, Z. Tian, Study on crack scattering in aluminum plates with Lamb wave frequency-wavenumber analysis, Smart Mater. Struct. 22 (2013) 065019.

[28] E.B. Flynn, S.Y. Chong, G.J. Jarmer, J.R. Lee, Structural imaging through local wavenumber estimation of guided waves, NDT and E Int. 59 (2013) 1-10.

[29] M.D. Rogge, C.A. Leckey, Characterization of impact damage in composite laminates using guided wavefield imaging and local wavenumber domain analysis, Ultrasonics 53 (2013) 1217-1226.

[30] A.S. Purekar, D.J. Pines, S. Sundararaman, D.E. Adams, Directional piezoelectric phased array filters for detecting damage in isotropic plates, Smart Mater. Struct. 13 (2004) 838.

[31] A.S. Purekar, D.J. Pines, Damage detection in thin composite laminates using piezoelectric phased sensor arrays and guided lamb wave interrogation, J. Intell. Mater. Syst. Struct. 21 (2010) 995-1010.

[32] Y. Wang, S. Yuan, L. Qiu, Improved wavelet-based spatial filter of damage imaging method on composite structures, Chinese J. Aeronaut. 24 (2011) 665-672.

[33] B. Xu, V. Giurgiutiu, Single mode tuning effects on lamb wave time reversal with piezoelectric wafer active sensors for structural health monitoring, J. Nondestruct. Eval. 26 (2007) 123-134.

[34] P.D. Wilcox, Omni-directional guided wave transducer arrays for the rapid inspection of large areas of plate structures, IEEE Trans. Ultrason. Ferroelectr. Freq. Control 50 (2003) 699-709.

[35] C.A. Balanis, Antenna Theory Analysis and Design, John Wiley, Hoboken, NJ, 2005.

[36] A. Velichko, P.D. Wilcox, Guided wave arrays for high resolution inspection, J. Acoust. Soc. Am. 123 (2008) 186-196.

[37] L. Qiu, S. Yuan, On development of a multi-channel PZT array scanning system and its evaluating application on UAV wing box, Sensor. Actuat. A-Phys. 151 (2009) 220-230.